Aminopolymer-functionalized hollow carbon spheres incorporating Ag nanoparticles for electrochemical syngas production from CO_2

Kaining Li [a], Yasutaka Kuwahara [a,b,*], Hiromi Yamashita [a,b]

[a] *Division of Materials and Manufacturing Science, Graduate School of Engineering, Osaka University, 2-1 Yamada-oka, Osaka 565-0871, Japan*
[b] *Innovative Catalysis Science Division, Institute for Open and Transdisciplinary Research Initiatives (OTRI), Osaka University, 2-1 Yamada-oka, Suita, Osaka 565-0871, Japan*

A B S T R A C T

Electrochemical CO_2 reduction (CO_2RR) to produce syngas (CO and H_2) is a highly attractive way for achieving carbon neutrality. However, it remains a challenge due to the lack of high-efficiency electrocatalysts that enables controllable CO/H_2 ratio syngas production. Herein, aminopolymer functionalized hollow carbon spheres incorporating Ag NPs (Ag-P@HCS) are developed, which function as active catalysts for syngas electrosynthesis. The introduction of aminopolymers results in finely improved dispersion of Ag NPs and increased CO_2 adsorption of Ag-P@HCS, thereby altering its CO_2RR performance. As a result, Ag-P@HCS achieves a 4.6-fold increase in the Faradaic efficiency of CO when compared to the amiopolymer-free analog (Ag-HCS) at -0.8 V vs. RHE. More importantly, the controllable CO/H_2 ratios (1.09 – 2.54) can be obtained for Ag-P@HCS over a wide potential window, which is capable of meeting the specific requirements for industrial production. This work demonstrates the potential of aminopolymer functionalization for designing high-performance CO_2RR electrocatalysts.

1. Introduction

Excessive fossil fuel consumption leads to an ever-increasing atmospheric carbon dioxide (CO_2) level and may cause catastrophic climate change. Attaining carbon neutrality via CO_2 reduction is a persistent objective of global sustainability. Integrating renewable energy, electrocatalytic CO_2 reduction (CO_2RR) provides a promising solution for achieving both net CO_2 elimination and value-added fuel production. Amongst the various CO_2RR products, syngas (the mixture of CO and H_2) is an ideal feedstock in synthetic chemical industry [1,2]. Currently, syngas is mainly produced by traditional technologies, including coal gasification, natural gas steam reforming, and reverse water–gas shift reactions, which involve energy-intensive procedures and harsh reaction conditions [3–5]. In contrast, electrosynthesis of syngas under mild conditions without geographical restrictions, using only CO_2 as a carbon source and H_2O as a hydrogen source, can provide a flexible platform for downstream industrial application (e.g., Fischer-Tropsch synthesis) [6–8]. While encouraging progress has been witnessed, several challenges remain. For instance, the yield of the reduction product CO is constrained by the chemical inertness of CO_2 molecule due to its large Gibbs free energy [9,10]. Furthermore, practical industrial production

requires specific ratios of syngas, especially in the range of 0.25–3.33 CO/H_2 [11]. Therefore, it is essential to develop efficient electrocatalysts for the controllable synthesis of syngas.

Among the numerous metal catalysts reported to date, Ag nanoparticles (NPs) were found to be effective catalysts for electrochemical CO_2-to-CO conversion because of their suitablebinding strength with CO [12,13]. However, their further application is limited due to the unsatisfactory CO_2 adsorption capacity. Aminopolymers containing abundant amine sites with high basicity are one of the best CO_2 capture candidates [14,15]. Previous studies have demonstrated that aminopolymers can be used in a variety of catalytic applications, such as thermocatalytic CO_2 hydrogenation for formate production [16] and photocatalytic CO_2 reduction for methanol synthesis [17], where aminopolymers assist in stabilizing metal NPs and the construction of local microenvironments with high CO_2 concentration around the active sites, resulting in improved catalytic efficiency. They are likewise expected to function as co-catalysts for optimizing the electrocatalytic CO_2 reduction performance [18]. Zhang et al. reported a polyethyleneimine (PEI)-coated nitrogen-doped carbon nanotube material that offered a significantly enhanced formate selectivity with a Faradaic efficiency of 85.0% compared to its PEI-free analog (59.0%) at -1.8 V vs. SCE, as a

---

result of the accelerated reaction kinetics induced by PEI [19]. Additionally, Li and co-workers revealed that PEI could stabilize the reaction intermediates by H-bonding or electrostatic interactions, allowing MoSx/PEI-modified rGO to improve the CO_2RR activity and change the CO/H$_2$ ratio [20]. Hence, the integration of aminopolymers with high CO_2 adsorption capacity and catalytically active sites is expected to provide a feasible solution to enhance the electrochemical CO_2 conversion efficiency and achieve the ratio variation of syngas components.

Recently, hollow carbon spheres (HCS) have become attractive candidate supports in the field of electrocatalysis, because of the characteristics of carbon and hollow-structured materials [21–25]. Specifically, hollow carbon spheres have the following advantages: (1) they provide cavity spaces that can accommodate various catalytic active materials (including metal NPs, oxides, MOFs, etc.); (2) their superior conductivity ensures rapid electron transfer; (3) the abundant pore structure allows the mass transfer of target molecules [26,27]. The positive effects of hollow carbon spheres in CO_2RR have been verified by some studies. For example, Liu et al. reported a HCS encapsulating Ni NPs catalyst, which exhibited a Faradaic efficiency (FE) of 93.2% for CO at pH 7.2, and 84.3% FE$_{CO}$ even at an acidic condition (pH 2.5), due to the nano-confining effects of HCS and the resulting inhibited proton diffusion [28]. Additionally, a recent study showed that the hollow nanostructure of HCS and constructed Cu/carbon interface allow for efficient mass transfer and charge transmission, thereby achieving high selectivity and remarkable stability for CO_2RR [29]. Given the as-mentioned advantages of HCS in metal-carbon systems, it can be anticipated to function as a robust support for designing high-performance heterogeneous electrocatalysts.

Along this line, herein, a nanostructured catalyst consisting of hollow carbon spheres incorporating Ag NPs and aminopolymers (Ag-P@HCS) is developed, which serves as an efficient catalyst for electrochemical syngas production from CO_2. Detailed characterizations demonstrate the incorporation of aminopolymers improves the dispersion of Ag NPs and enhances CO_2 absorption. As a result, Ag-P@HCS shows a significantly improved Faradaic efficiency (FE) of 70.1% for CO at − 0.8 V vs. RHE, as compared to the aminopolymer-free analog (Ag-HCS, FE$_{CO}$ = 15.3%). Additionally, the controllable CO/H$_2$ ratios (1.09 – 2.54) can be obtained for Ag-P@HCS over a wide window potential from − 0.7 V to − 1.1 V vs. RHE.

2. Experimental section

2.1. Chemical reagents

Carbon tetrachloride (CCl$_4$) was purchased from Fujifilm Wako Pure Chemical Corporation (Japan). Tetrapropyl orthosilicate (TPOS), absolute ethanol (EtOH, 99.5%), resorcinol (*m*-dihydroxybenzene, 99%), formaldehyde solution (formalin, 37%), ammonia solution (NH$_3$·H$_2$O, 28%), sodium hydroxide (NaOH, 97%), ethylenediamine anhydrous (C$_2$H$_8$N$_2$, 98%), silver nitrate (AgNO$_3$, 99.8%), sodium borohydride (NaBH$_4$) and Potassium hydrogen carbonate (KHCO$_3$) were purchased from Nacalai Tesque Inc. (Japan). All chemicals were used as received without further treatment. Deionized (DI) water was supplied from local source, and used throughout the experiment.

2.2. Synthesis of hollow carbon sphere (HCS)

Hollow carbon spheres were prepared via a modified template method [30]. Typically, TPOS and resorcinol formaldehyde (RF) were used to synthesize silica cores and RF oligomer overlayers, respectively, to obtain core-shell SiO$_2$@RF nanostructure. Specifically, 3.5 mL of TPOS was dropwise added to the reaction solution comprising 10 mL of distilled water, 70 mL of absolute ethanol, and 3 mL of ammonia solution under magnetic stirring for 20 min. After that, 0.4 g of resorcinol and 0.56 mL of formaldehyde were added to the solution, then, the mixture was maintained stirring for 24 h. The resulting orange

precipitate was washed thoroughly with DI water and ethanol. After being dried at 80 °C overnight, the precipitate was calcined at 700 °C (heating ramp rate = 2 °C min^{-1}) in a tube furnace for 5 h under N$_2$ flow (100 mL min^{-1}) to prepare SiO$_2$@C nanospheres. Eventually, the hollow carbon spheres (HCS) were obtained by dissolving the interior SiO$_2$ particles with 4 M NaOH solution under stirring for 24 h at room temperature.

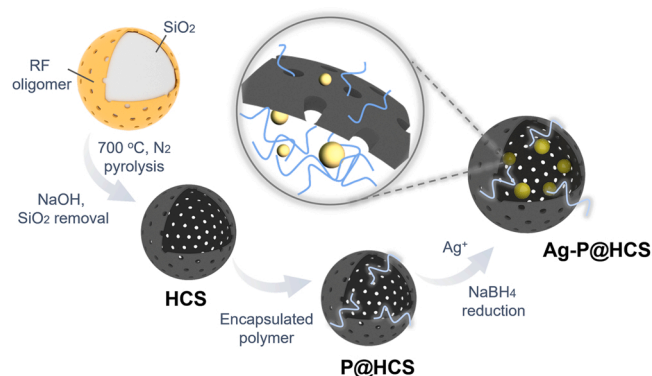### 2.3. Synthesis of aminopolymer@hollow carbon sphere (P@HCS)

The typical synthesis of P@HCS is described below, in which aminopolymer was prepared via a representative synthesis method using ethylenediamine and carbon tetrachloride as precursors [31]. 0.5 g of HCS powder was added to the mixture of 0.675 g of ethylenediamine and 1.5 g of carbon tetrachloride and stirred in an oil bath at 90 °C for 6 h. The precipitate was then centrifuged and washed with DI water and ethanol ca. 10 times until the supernatant turned colorless, followed by a vacuum drying at room temperature to obtain aminopolymer@hollow carbon spheres (P@HCS). For comparison, three control samples (*x*P@HCS, *x* = 0.5, 2, 4) with different polymer contents were also prepared; *x* represents the different volume ratios of ethylenediamine and carbon tetrachloride compared to that of P@HCS.

2.4. Synthesis of Ag NPs-aminopolymer@hollow carbon sphere (Ag-P@HCS)

To obtain Ag-P@HCS, 0.1 g of P@HCS powder was first soaked in 6.30 mL of AgNO$_3$ aqueous solution (5 mg mL^{-1}) and ultrasonicated for 20 min, followed by a magnetic stir for 24 h at room temperature. Afterward, 7.42 mL of freshly prepared aqueous NaBH$_4$ solution (0.5 mol L^{-1}) was dropwise added to the above suspension under stirring at room temperature, enabling the Ag$^+$ reduction process to form Ag NPs. After 1 h stirring, the obtained powder was washed 3 times with DI water and ethanol, respectively. After being dried in a vacuum at room temperature overnight, the Ag-P@HCS was obtained. The control samples (Ag-0.5P@HCS, Ag-2P@HCS and Ag-4P@HCS) were prepared using the same method.

2.5. Characterization

X-ray diffraction (XRD) diffractograms of the as-synthesized samples were recorded on an X-ray diffractometer (Rigaku Ultima IV) with a Cu Kα radiation source (λ = 1.54056 Å). The morphology and microstructure observations were performed via transmission electron microscopy (TEM, H-800 Hitachi) and a high-angle annular dark field scanning/transmission electron microscopy (HAADF-STEM, JEOL ARM200F), respectively; and the corresponding energy dispersive X-ray spectroscopy element mapping (EDS mapping) was obtained on the aforementioned HAADF-STEM apparatus. The field emission scanning electron microscopy (FE-SEM) images were collected on JEOL JIB-4610 F. Nitrogen adsorption-desorption isotherms were acquired by a nitrogen adsorption-desorption system (BEL BELSORP-max, Micromeritics) at − 196 °C; samples were pretreated at 120 °C under vacuum for 6 h before the measurement to exclude the effects of water. Specifically, the specific surface area (analyzed from the adsorption data in the p/p_0 range of 0.05–0.30) and the pore size distribution were calculated using Brunauer-Emmett-Teller (BET) method and Barrett-Joyner-Halenda (BJH) method, respectively. Thermogravimetric (TG) measurements were conducted on a Rigaku thermogravimetry unit with a Rigaku Thermo Plus EVO II series high-temperature differential thermal balance, within the temperature range from 50 °C to 700 °C. CO_2 uptake kinetics curves were also recorded using the TG thermogravimeter at 40 °C under a flow of 10% CO_2/N$_2$. The synchrotron radiation experiments for XAFS measurements were performed at the BL01B1 beam line in SPring-8 facility, JASRI, Harima, Japan, with approval from JASRI (no. 2022A1171). Prior to measurements, the sample pellets used for Ag

Scheme 1. Synthesis procedure of aminopolymer-modified hollow carbon spheres incorporating Ag nanoparticles (Ag-P@HCS).

K-edge XAFS measurements were prepared by diluting the catalysts with high-purity boron nitride. The Ag K-edge XAFS spectra of all samples were recorded in transmission mode. Data analyses were carried out on the ATHENA software package. To acquire the radial structure functions, Fourier transformation of the k^3-weighted normalized EXAFS data was performed over the range of $3.0 < k$ (Å^{-1}) < 12.0. X-ray photoelectron spectra (XPS) were collected on a photoelectron spectrometer (ESCA-3400, Shimadzu), with Mg Kα radiation (hν =1253.6 eV) as the excitation source. All the binding energies of elements were calibrated with the C 1 s peak at 284.5 eV from adventitious carbon.

2.6. Electrochemical measurements

The electrochemical experiments were performed in a three-electrode system with an electrochemical workstation (HZ-7000, Hokuto Denko) at room temperature using an air-tight two-compartment cell separated by a proton exchange membrane (Nafion 117, Dupont). Platinum wire and Ag/AgCl electrodes were employed as

counter and reference electrodes, respectively. To prepare the working electrode, 10 mg of catalyst was dispersed in the mixture containing 1 mL of ethanol and 50 μL Nafion solution (5 wt%). After being ultrasonicated for 30 min, 100 μL of the homogeneous ink was pipetted onto a 1.0×1.0 cm^2 carbon cloth with a mass loading of 1 mg cm^{-2}. 70 mL of 0.5 M KHCO$_3$ electrolyte was filled in each cell, leaving 48 mL headspace. The potentials measured against Ag/AgCl were calibrated to the reversible hydrogen electrode (RHE) in accordance with the Nernst function (E (vs. RHE) = E (vs. Ag/AgCl) + 0.197 V + 0.059 × pH).

Prior to the electrochemical measurements, high-purity CO$_2$ was bubbled into the electrolytes in both cathodic and anodic chambers for 30 min at a flow rate of 20 mL min^{-1}. The pH value of the CO$_2$-saturated 0.5 M KHCO$_3$ solution was measured to be 7.48. To determine the products and the referred Faradaic efficiencies (FEs), the constant potential electrolysis was conducted at each potential for 30 min. Subsequently, 200 μL of the gaseous product was taken from the gas headspace of the cathode compartment using a gas-tight syringe (Hamilton). The quantifications of gas products were performed on a gas chromatography apparatus (GC-8A, Shimadzu) with a flame ionization detector (FID) and a methanizer (MTN-1, Shimadzu) equipped with an active carbon column. The electrolyte after the reaction was collected and examined on a high-performance liquid chromatography (HPLC, Shimadzu) system with an ion-exclusion column (300 × 7.8 mm, Bio-Rad Aminex HPX-87 H) using 5 mM H$_2$SO$_4$ aqueous solution as the mobile phase with a flow rate of 0.5 mL min^{-1}. In this work, no liquid product signal was observed in HPLC spectra. The Faradaic efficiency of gas products is calculated via equation FE = mF × n/Q [32], where m is the transferred electron numbers to generate target product (m = 2 for CO and H$_2$); F is the Faradaic constant (96,485 C mol^{-1}); n (unit: mol) is the amount of each product; Q represents the total amount of charge consumed during the electrolysis process. The electrochemically active surface area (ECSA) was estimated from the electrochemical capacitance (Cdl) by conducting cyclic voltammetry (CV) test in a certain potential window within the non-Faradaic region at different scan rates (20, 30, 40, 50, 60 mV s^{-1}). The electrochemically active surface area (ECSA) is
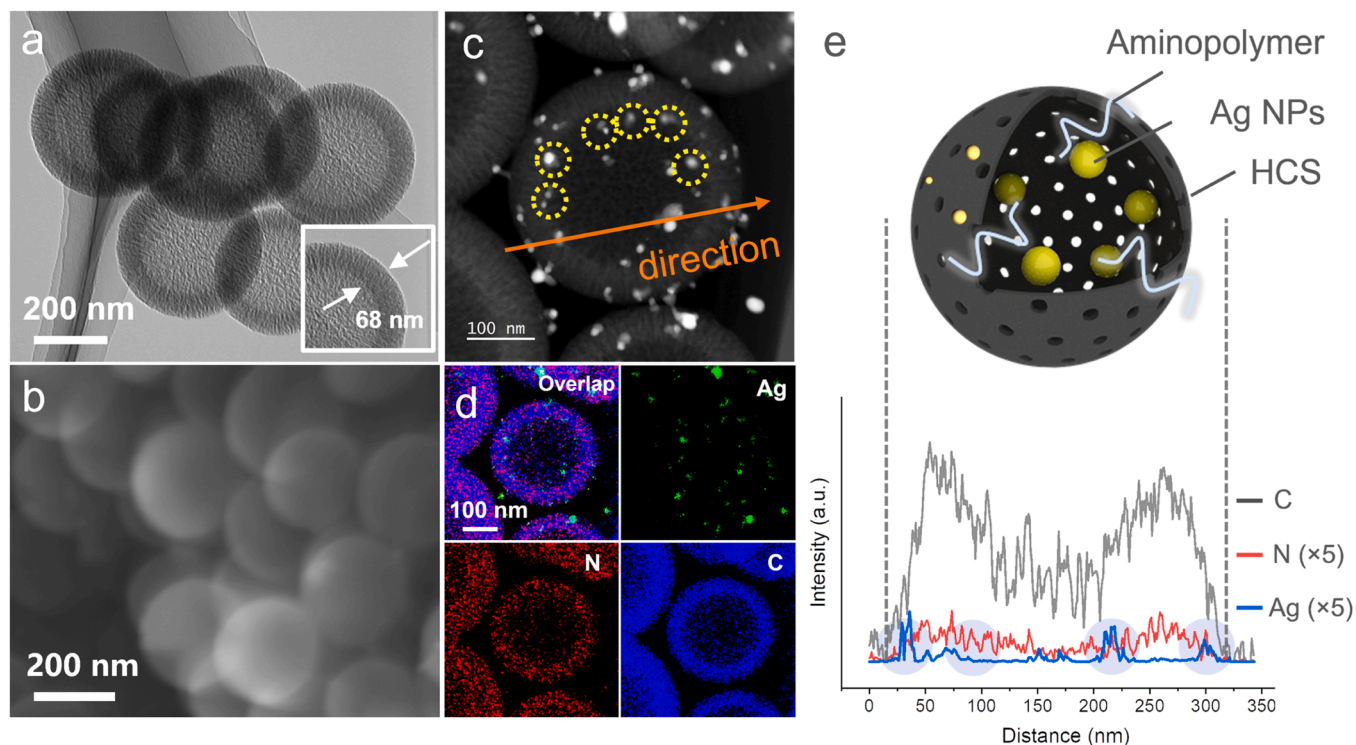

Fig. 1. (a) TEM image of HCS. (b) FE-SEM, (c) HAADF-STEM, and (d) the corresponding EDS mapping images of Ag-P@HCS. (e) Structural illustration and elemental line scan across a Ag-P@HCS composite along with the direction shown in (c).
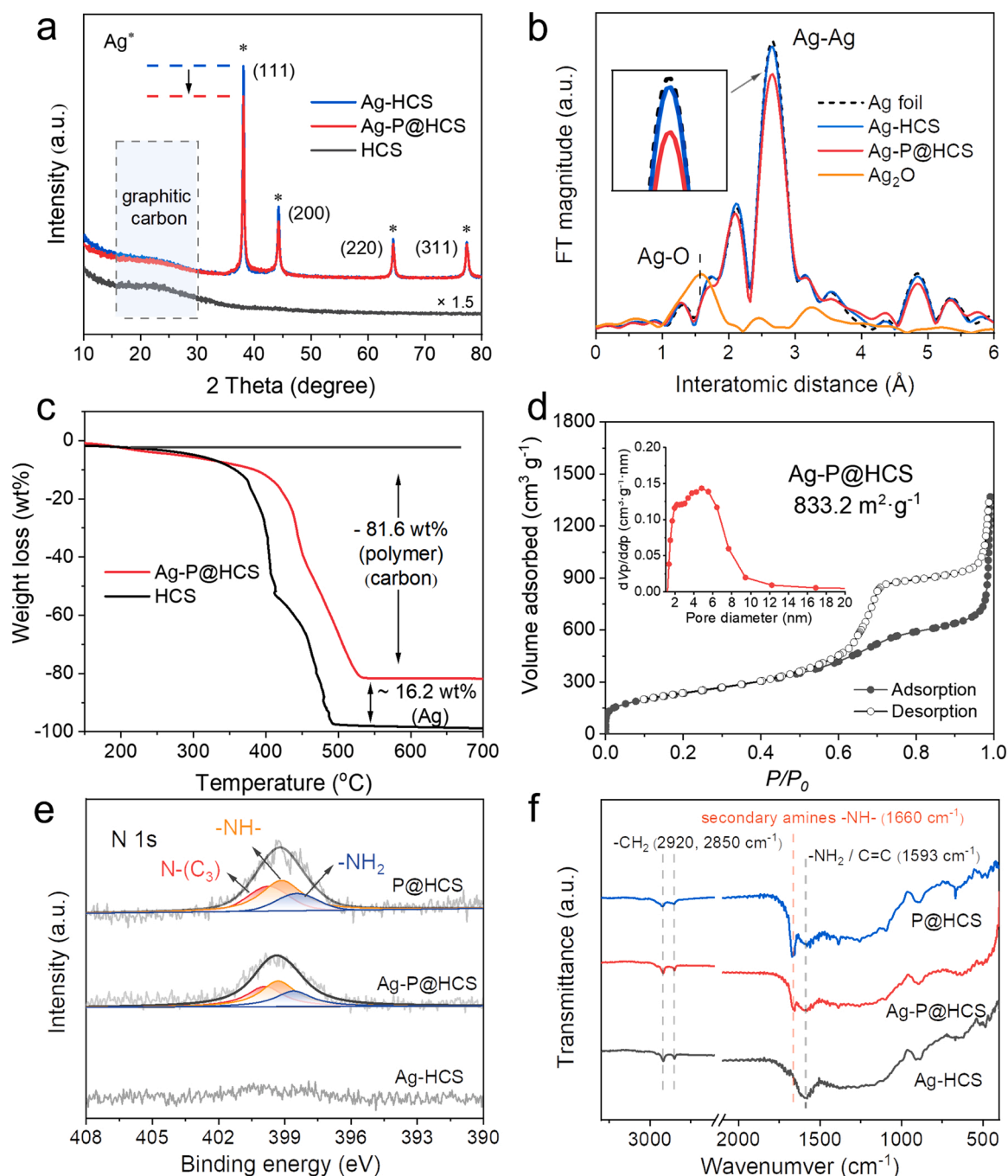
Fig. 2. (a) XRD diffractograms of HCS, Ag-HCS, and Ag-P@HCS. (b) FT-EXAFS spectra of Ag K-edge for Ag-HCS and Ag-P@HCS, with Ag foil and Ag$_2$O as comparisons. (c) Weight loss curve and (d) N$_2$ adsorption-desorption isotherms of Ag-P@HCS (Inset of Fig. 2d: the BJH pore distribution curve). (e) N 1 s XPS spectra and (f) FTIR spectra of Ag-HCS, Ag-P@HCS and P@HCS.

positively correlated with Cdl according to the formula: ECSA = Cdl/Cs (Cs is the specific capacitance constant) [33,34]. The Cdl can eventually be obtained via plotting the Δj ($j_a - j_c$)/2 at 0.15 V vs. Ag/AgCl against the scan rates, where j_a and j_c are the anodic and cathodic current densities, respectively. EIS measurements were carried out in 0.5 M KHCO$_3$ solution at the open-circuit potential with an AC amplitude of 10 mV over a range of 0.01 Hz to 100 kHz.

3. Results and discussion

3.1. Physicochemical properties of as-prepared samples

Scheme 1 shows the synthesis procedures of Ag-P@HCS. To begin with, the core-shell SiO$_2$@resorcinol-formaldehyde (RF) oligomer spheres were prepared via a commonly used Stöber method [30]. wherein SiO$_2$ and RF acted as templates and carbon precursors, respectively. Then, through pyrolytic carbonization of shell organics, followed by NaOH etching of SiO$_2$ cores, hollow carbon spheres (HCS) were acquired (Fig. 1a and Fig. S1). The shell thickness of HCS is about 68 nm, and the disordered mesoporous channel structure can be
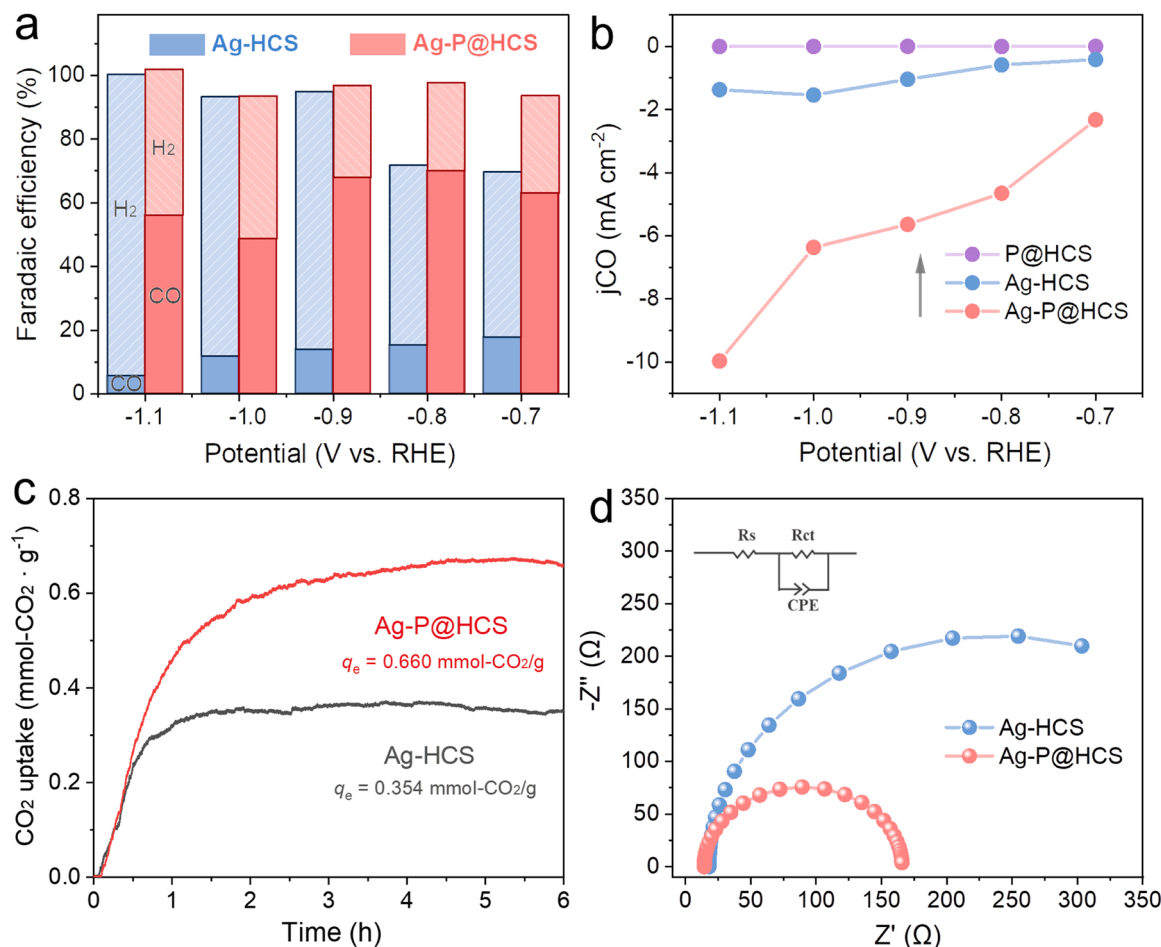
Fig. 3. (a) Faradaic efficiencies for CO and H_2 production and (b) CO partial current density (J_{CO}) at the given potentials over as-prepared samples. (c) Kinetics in CO_2 adsorption in a flow of 10% CO_2/N_2 at 40 °C and (d) EIS spectra over Ag-HCS and Ag-P@HCS.

observed in the shell (inset of Fig. 1a). Subsequent in-situ polymerization of ethylenediamine and carbon tetrachloride yielded aminopolymers, which were encapsulated in HCS (P@HCS) [31]. Lastly, Ag-P@HCS was prepared by adding $NaBH_4$ reductant to reduce Ag^+ ions in the P@HCS dispersed in an aqueous suspension (all synthetic details are given in the experimental section).

The structural features and chemical compositions of Ag-P@HCS are revealed by scanning electron microscopy (SEM), scanning transmission electron microscopy (STEM), and energy dispersive spectroscopy (EDS) mapping. Ag-P@HCS displays a large internal cavity in the spherical structure (Fig. 1b and c), and the Ag NPs are homogeneously dispersed on the inner wall (yellow dashed circle in Fig. 1c) and outside shell of the hollow carbon sphere, as evidenced by the EDS results (Fig. 1d). Additionally, the TEM image shows that Ag-P@HCS has a small Ag NPs average size of 10.8 nm (Fig. S2). In contrast to Ag-P@HCS, the Ag NPs on Ag-HCS (aminopolymer-free sample) appear to be aggregated easily to form larger NPs (Fig. S3 a, b). This indicates that there might be an interaction between Ag atoms and aminopolymers during the metal nucleation process, resulting in the well-distributed Ag NPs on Ag-P@HCS [30]. The EDS mapping analysis allows to visualize the elemental distribution of Ag-P@HCS. As shown in Fig. 1d, the N and C atoms are localized at the same region, suggesting the spatial proximity between aminopolymer and carbon shell. Besides, the green spots representing Ag NPs can be clearly seen. Careful observation by line scan mapping profiles (Fig. 1e) of a selected Ag-P@HCS composite (orange line in Fig. 1c) confirms that the Ag NPs are dispersed around the carbon shell region.

The crystallographic structures of as-prepared samples were

scrupulously identified by X-ray diffraction (XRD) patterns. As shown Fig. 2a, both Ag-HCS and Ag-P@HCS display four distinct diffraction peaks associated with metallic Ag (JCPDS card 04–0783), while a faint broad peak at 2 Theta value of 24.9° is assigned to graphitic carbon (002) facet that originates from HCS. Notably, as compared with Ag-HCS, a decreased peak intensity of Ag in Ag-P@HCS can be observed, implying the lower crystallinity states for Ag NPs due to the increased dispersion and smaller size of Ag NPs (Fig. S2 and S3).

X-ray absorption fine-structure (XAFS) spectroscopy was employed to examine the local structure of Ag atoms. The shapes and edge positions in Ag K-edge X-ray absorption spectra of Ag-P@HCS and Ag-HCS were similar to those of reference Ag foil (Fig. S4), confirming that Ag species dominantly existed in metallic Ag state, as evidenced by the XPS spectra of Ag 3d (Fig. S5). Furthermore, in the Fourier transforms of extended XAFS spectrum (FT-EXAFS) for Ag K-edge (Fig. 2b), Ag-P@HCS and Ag-HCS showed Ag-Ag scattering peaks at 2.66 Å, whereas no Ag-O bond (1.55 Å) appeared, which excludes the presence of oxidized Ag species [35,36]. Noteworthily, the decreased Ag-Ag peak further verified smaller Ag NPs are formed on Ag-P@HCS compared to those of Ag-HCS. The mass ratio of Ag species in Ag-P@HCS determined by thermogravimetry (TG) analysis was about 16.2 wt% (Fig. 2c), whereas HCS showed a weight loss of 97.8 wt% up to 500 °C, ascribing to the thermal combustion of carbon.

The specific surface area and pore characteristic of the as-synthesized samples were determined by N_2 adsorption–desorption analysis. As shown in Fig. 2d, Ag-P@HCS exhibits a typical type-IV N_2 sorption isotherm with a large hysteresis in the range of $0.6 < p/p_0 < 1.0$, suggesting the presence of hollow cavity spaces [30]. The
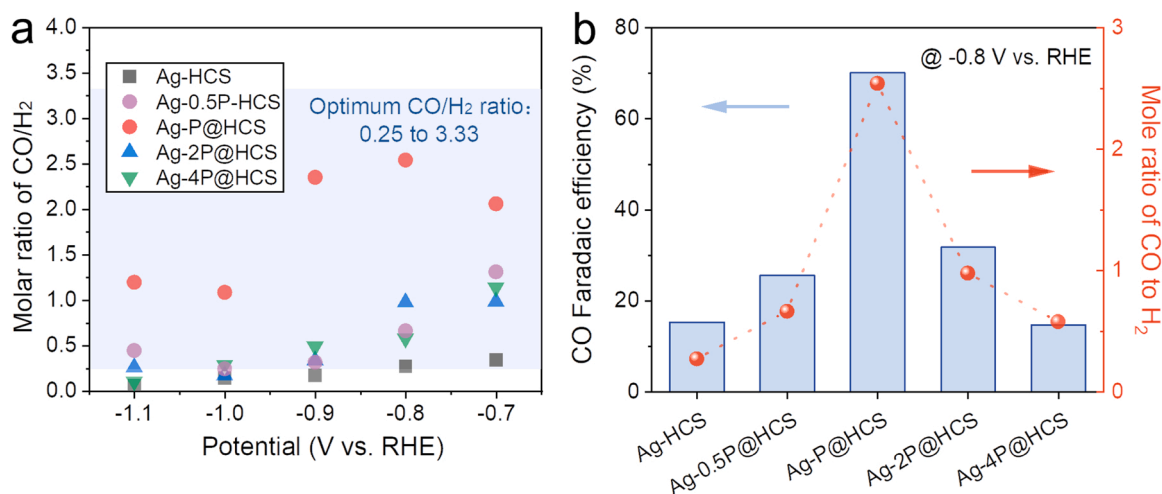
Fig. 4. (a) Molar ratio of CO/H_2 in the product gas over as-synthesized catalysts. (b) CO FEs and CO/H_2 molar ratios over Ag-xP@HCS at -0.8 V vs. RHE.

corresponding pore size distribution result reveals the existence of abundant mesopores on Ag-P@HCS (peak pore diameter: 4.8 nm), which should mainly be originated from the hollow carbon shell. It should be noted that the large specific surface area of 883.2 $m^2\,g^{-1}$ and the rich pore nature of Ag-P@HCS permit the reactants to access the active sites (See Table S1 for more details).

XPS spectra of N 1 s (Fig. 2e) of Ag-P@HCS and P@HCS showed the characteristic peaks of =N-, -NH-, and $-NH_2$ attributed to the amine sites on aminopolymer [37]; while no signal was observed in the N 1 s spectrum of Ag-HCS. In FTIR spectra (Fig. 2f), all samples exhibited peaks at both 2920 and 2850 cm^{-1}, which attributed to asymmetric and symmetric stretching vibration bonds of $-CH_2$, respectively [38]. In comparison to Ag-HCS, distinct peaks resulting from the -NH- stretching vibration in the aminopolymer were observed at 1660 cm^{-1} for Ag-P@HCS and P@HCS [39]. The peaks observed at 1593 cm^{-1} were ascribed to the overlapping bands of the stretching vibrations of $-NH_2$ and C=C [40,41]. In conjunction with the above XPS and FTIR results, it can be asserted that aminopolymers were successfully introduced into Ag-P@HCS.

3.2. Electrocatalytic CO_2 reduction performance

The CO_2RR performances of as-synthesized samples were evaluated in CO_2-saturated 0.5 M $KHCO_3$ solution using a gas-tight H-type cell equipped with a standard three-electrode setup (Fig. S6). The reduction products are quantitatively analyzed utilizing gas chromatography. H_2 is the main electrolysis product for P@HCS, with barely CO being produced (Fig. S7). Different from P@HCS, samples containing Ag nanoparticles (i.e., Ag-HCS and Ag-P@HCS) demonstrate a certain efficiency in CO production (Fig. 3a). It can be inferred that Ag NPs can serve as the active sites for CO generation, which associates with the relatively weak binding strength with CO, as experimentally and theoretically verified in previous researches [12,13,42–44]. Compared with Ag-HCS, a much higher FE_{CO} can be observed over Ag-P@HCS at all potentials (Fig. 3a); and the highest FE_{CO} of Ag-P@HCS reaches 70.1% at -0.8 V vs. RHE, which is 4.6 times higher than the value of Ag-HCS (15.3%). Furthermore, Ag-P@HCS exhibits the largest CO partial current density (j_{CO}) among these samples (Fig. 3b), which is an indication of the positive effects on electroactivity induced by aminopolymer. With the increase of negatively applied potential, the CO Faradaic efficiencies of Ag-HCS and Ag-P@HCS are decreased due to the restrained CO_2RR caused by the limitation of CO_2 mass transport; in contrast, the H_2 Faradaic efficiencies of the samples show upward trends since the hydrogen evolution is less affected by the proton transport [45].

It has been widely recognized that CO_2 adsorption and intermediate

$CO_2^{\bullet-}$ stabilization of electrocatalysts are the important influence factors for CO_2-to-CO conversion [9,46]. In a gaseous CO_2 adsorption measurement, Ag-P@HCS exhibited a higher CO_2 uptake capacity (0.66 mmol-CO_2/g), which was 1.8-fold higher than the value of its aminopolymer-free counterpart (Ag-HCS, 0.354 mm-CO_2/g) (Fig. 3c). This is because aminopolymer containing a large amount of amines group is typically capable of capturing CO_2 molecules [16,47], leading to the boosted CO_2 adsorption. The binding affinity of intermediate $CO_2^{\bullet-}$ of the samples was evaluated using OH^- ion as a substitute via oxidative LSV scanning in N_2-bubbled 0.1 M NaOH electrolyte [48–50]. A lower OH^- adsorption potential was observed on Ag-P@HCS as compared with Ag-HCS (Fig. S8), indicating that Ag-P@HCS possesses a stronger OH^- adsorption ability. Thus, it is conceived that the aminopolymer favors the stabilization of $CO_2^{\bullet-}$ intermediate and results in an accelerated electrocatalytic CO_2-to-CO process, in line with the enhanced catalytic performance. Moreover, Ag-P@HCS (R_{ct} = 151.4 Ω) shows a much smaller arc radius of the Nyquist plot compared to Ag-HCS (R_{ct} = 439.5 Ω) (Fig. 3d), indicating the lower electron-transfer resistance and the resulting fast charge-transfer process occurring on Ag-P@HCS [51–54], which is related to the good dispersion of Ag NPs associated with the introduction of aminopolymer. More importantly, Ag-P@HCS shows good long-term stability, as illustrated in the i-t curve of 16 h continuous test at -0.8 V vs. RHE (Fig. S9). The recycled Ag-P@HCS after long-term measurement was investigated by TEM (inset in Fig. S9), which verified that the hollow structure morphology was well maintained. This result indicates the satisfactory durability of the Ag-P@HCS owing to the confinement effect of HCS.

For further comparison, Ag-0.5P@HCS, Ag-2P@HCS and Ag-4P@HCS samples with varying polymer contents were synthesized (see the experimental section for details) [30]; XRD, FTIR, and EXAFS results confirmed the compositions and structures of control samples were similar to those of Ag-P@HCS (Fig. S10a, b, and c). The effects of polymer amount on CO/H_2 production ratio from electrochemical CO_2 reduction were evaluated at different potentials. The CO and H_2 production rates of most samples increased from -0.7 V to -1.1 V, being highly dependent on the applied potentials, as depicted in Fig. S11a and b. Among them, Ag-P@HCS showed the highest CO production rate, with the CO production rate increasing from 43.4 μmol h^{-1} cm^{-1} (-0.7 V) to 186.0 μmol h^{-1} cm^{-1} (-1.1 V), while the H_2 production rate was maintained at a relatively low value.

Fig. 4a presents the CO/H_2 syngas evolution ratio of the as-prepared catalysts. The blue region indicates the optimum CO/H_2 ratio (0.25–3.33) for industrial applications [11]. Different from the other samples, the value of CO/H_2 ratio for Ag-P@HCS (1.09–2.54) can be controlled within the optimal syngas ratio range with a wide potential
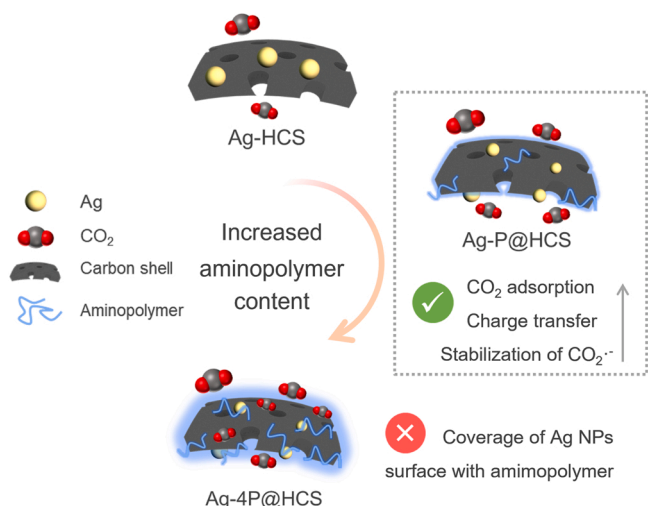
Fig. 5. Schematic illustration of the structure and CO_2RR performance variation of Ag-P@HCS with increased aminopolymer content.

window, which is suitable for down-stream Fischer-Tropsch and fermentation processes. For further comparison, the syngas production performances of Ag-xP@HCS with other representative electrocatalysts reported in the literature were summarized (Table S2). It suggests that Ag-P@HCS is one of the most competitive syngas-producing composite catalysts with a wide potential range. Additionally, adjustable CO/H_2

molar ratios can be obtained at the potential of -0.8 V for Ag-HCS (0.27), Ag-0.5P@HCS (0.66), Ag-P@HCS (2.54), Ag-2P@HCS (0.98) and Ag-4P@HCS (0.58) (Fig. 4b), due to the varied aminopolymer content. As previously discussed, Ag-P@HCS showed a much higher selectivity for CO production compared to Ag-HCS, due to the altered catalytic properties resulting from the increased Ag dispersion and enhanced CO_2 affinity after aminopolymer functionalization (Fig. 5). As for Ag-2P@HCS and Ag-4P@HCS, despite the increase of aminopolymer amount favoring CO_2 adsorption (Fig. S12), their FE_{CO} and CO/H_2 ratio values decreased in comparison to Ag-P@HCS. Based on the CV curve data measured at the non-Faradaic region (Fig. 6a-c), the electrochemically active surface areas (ECSA) of Ag-xP@HCS were calculated. As shown in Fig. 6d, the value of electrochemical double-layer capacitance (Cdl) decreases from 5.17 mF cm^{-2} (Ag-P@HCS) to 1.36 mF cm^{-2} (Ag-4P@HCS), indicating that the number of electrochemically active exposed sites declines conceivably because of the coverage of Ag NPs surface with the aminopolymer (Fig. 5). The declined CO_2RR performance leads to the change of CO/H_2 ratio. Therefore, it is crucial to tune the aminopolymer content to obtain a specific ratio of syngas production.

4. Conclusion

In summary, aminopolymer-functionalized hollow carbon spheres incorporating Ag NPs were developed to produce syngas with controllable CO/H_2 ratios from electrochemical CO_2 reduction. The introduction of aminopolymer contributes to a significant enhancement of the FE_{CO} of Ag-HCS, stemming from a combination of elevated CO_2
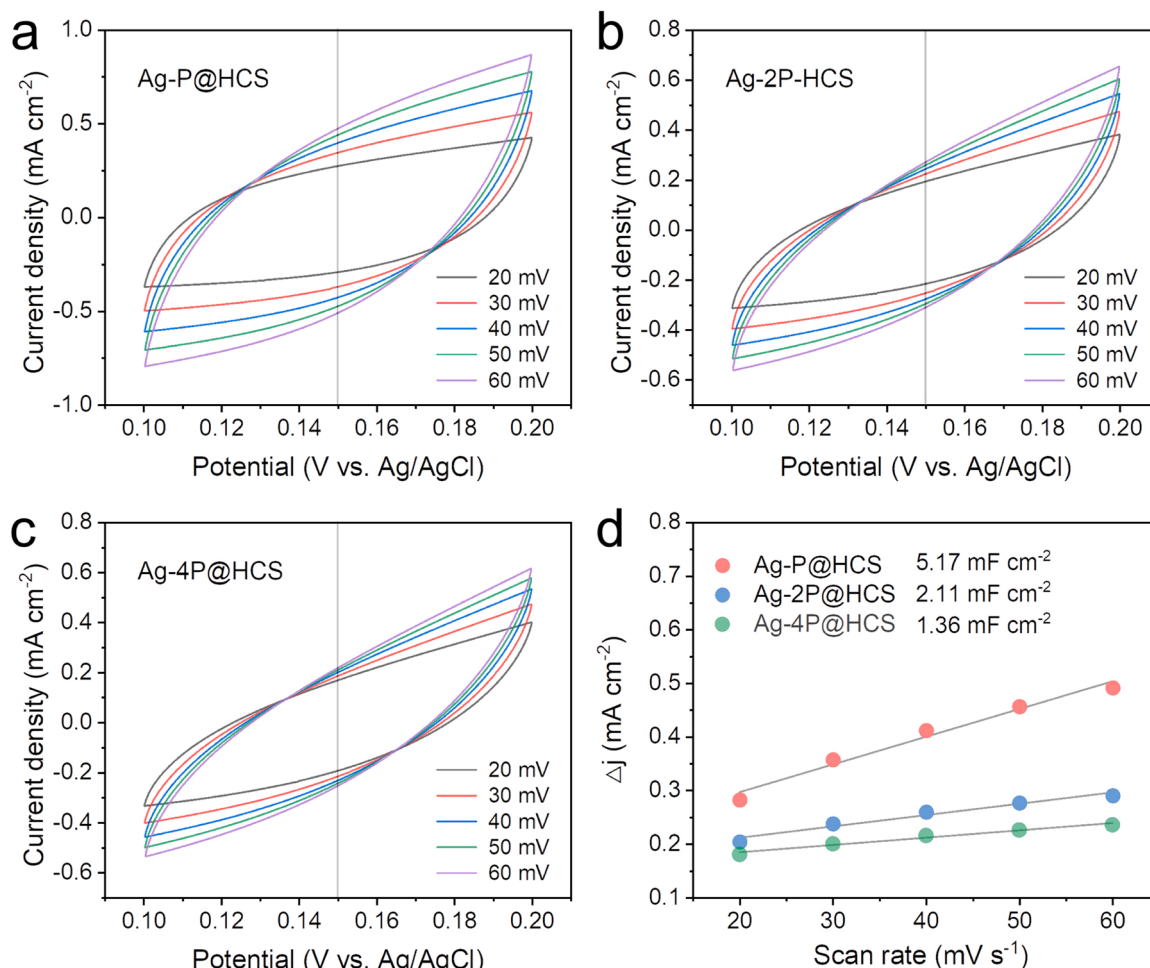

Fig. 6. CV curves of (a) Ag-P@HCS, (b) Ag-2P@HCS, and (c) Ag-4P@HCS. (d) Plots of charging current density differences (Δj) vs scan rates of Ag-xP@HCS samples.

adsorption ability, decreased charge transfer resistance as well as stabilization of the intermediate product ($CO_2^{\bullet-}$). By optimizing the aminopolymer inclusion in this catalytic system, appropriate syngas evolution ratios for industrial processes are anticipated. The findings highlight the roles of aminopolymer in this catalyst system, and may inspire the designing of high-performance electrocatalysts for green and sustainable energy conversion. Compared to the flow cell, the H-type cell used in this work is more suitable for studies focusing on high-performance electrocatalyst design and screening in comparison to the flow cell, given the ease of operation and rapid testing. However, for further widespread commercial application, the flow cell is more pragmatic because it can effectively overcome the mass transfer limitation in the case of H-cell setup , by ensuring a continuous flow of CO_2. High CO_2RR performance over this electrocatalyst can be expected by using the flow cell system in near future.

CRediT authorship contribution statement

Kaining Li: Data analysis, Investigation, Methodology, Data curation, Writing – original draft. **Yasutaka Kuwahara**: Conceptualization, Writing – review & editing, Theoretical direction, Funding acquisition. **Hiromi Yamashita**: Supervision, Writing – review & editing, Funding acquisition.

Declaration of Competing Interest

The authors declare the following financial interests/personal relationships which may be considered as potential competing interests: A co-author, Prof. Hiromi Yamashita, has been employed as an editor of Applied Catalysis B.

Data availability

The data that has been used is confidential.

Acknowledgments

Appendix A. Supporting information

Supplementary data associated with this article can be found in the online version at doi:10.1016/j.apcatb.2023.122713.

References

[1] Y. Xu, X. Li, J. Gao, J. Wang, G. Ma, X. Wen, Y. Yang, Y. Li, M. Ding, A hydrophobic FeMn@Si catalyst increases olefins from syngas by suppressing C1 by-products, Science 371 (2021) 610–613.

[2] G. Liu, G. Yang, X. Peng, J. Wu, N. Tsubaki, Recent advances in the routes and catalysts for ethanol synthesis from syngas, Chem. Soc. Rev. 51 (2022) 5606–5659.

[3] P. De Luna, C. Hahn, D. Higgins, S.A. Jaffer, T.F. Jaramillo, E.H. Sargent, What would it take for renewably powered electrosynthesis to displace petrochemical processes? Science 364 (2019) eaav3506.

[4] C. Han, Y.H. Li, J.Y. Li, M.Y. Qi, Z.R. Tang, Y.J. Xu, Cooperative syngas production and C−N bond formation in one photoredox cycle, Angew. Chem. Int. Ed. 60 (2021) 7962–7970.

[5] R. Daiyan, E.C. Lovell, B. Huang, M. Zubair, J. Leverett, Q. Zhang, S. Lim, J. Horlyck, J. Tang, X. Lu, K. Kalantar-Zadeh, J.N. Hart, N.M. Bedford, R. Amal, Uncovering atomic-scale stability and reactivity in engineered zinc oxide electrocatalysts for controllable syngas production, Adv. Energy Mater. 10 (2020) 1–9.

[6] Y. Ji, P. Gao, Z. Zhao, D. Xiao, Q. Han, H. Chen, K. Gong, K. Chen, X. Han, X. Bao, G. Hou, Oxygenate-based routes regulate syngas conversion over oxide–zeolite bifunctional catalysts, Nat. Catal. 5 (2022) 594–604.

[7] M.B. Ross, C.T. Dinh, Y. Li, D. Kim, P. De Luna, E.H. Sargent, P. Yang, Tunable Cu enrichment enables designer syngas electrosynthesis from CO_2, J. Am. Chem. Soc. 139 (2017) 9359–9363.

[8] J. Leverett, R. Daiyan, L. Gong, K. Iputera, Z. Tong, J. Qu, Z. Ma, Q. Zhang, S. Cheong, J. Cairney, R.S. Liu, X. Lu, Z. Xia, L. Dai, R. Amal, Designing undercoordinated Ni-Nx and Fe-Nx on holey graphene for electrochemical CO_2 conversion to syngas, ACS Nano 15 (2021) 12006–12018.

[9] N. Meng, C. Liu, Y. Liu, Y. Yu, B. Zhang, Efficient electrosynthesis of syngas with tunable CO/H2 ratios over ZnxCd1−xS-amine inorganic–organic hybrids, Angew. Chem. Int. Ed. 58 (2019) 18908–18912.

[10] E. Gong, S. Ali, C.B. Hiragond, H.S. Kim, N.S. Powar, D. Kim, H. Kim, S. Il In, Solar fuels: research and development strategies to accelerate photocatalytic CO_2 conversion into hydrocarbon fuels, Energy Environ. Sci. 15 (2021) 880–937.

[11] M.B. Ross, Y. Li, P. De Luna, D. Kim, E.H. Sargent, P. Yang, Electrocatalytic rate alignment enhances syngas generation, Joule 3 (2019) 257–264.

[12] C. Kim, H.S. Jeon, T. Eom, M.S. Jee, H. Kim, C.M. Friend, B.K. Min, Y.J. Hwang, Achieving selective and efficient electrocatalytic activity for CO_2 reduction using immobilized silver nanoparticles, J. Am. Chem. Soc. 137 (2015) 13844–13850.

[13] S. Liu, H. Tao, L. Zeng, Q. Liu, Z. Xu, Q. Liu, J.L. Luo, Shape-dependent electrocatalytic reduction of CO_2 to CO on triangular silver nanoplates, J. Am. Chem. Soc. 139 (2017) 2160–2163.

[14] H.J. Moon, J.M. Carrillo, J. Leisen, B.G. Sumpter, N.C. Osti, M. Tyagi, C.W. Jones, Understanding the impacts of support-polymer interactions on the dynamics of poly(ethyleneimine) confined in mesoporous SBA-15, J. Am. Chem. Soc. 144 (2022) 11664–11675.

[15] S.H. Pang, L.C. Lee, M.A. Sakwa-Novak, R.P. Lively, C.W. Jones, Design of aminopolymer structure to enhance performance and stability of CO_2 sorbents: poly(propylenimine) vs poly(ethylenimine), J. Am. Chem. Soc. 139 (2017) 3627–3630.

[16] Y. Kuwahara, Y. Fujie, T. Mihogi, H. Yamashita, Hollow mesoporous organosilica spheres encapsulating PdAg nanoparticles and poly(ethyleneimine) as reusable catalysts for CO_2 hydrogenation to formate, ACS Catal. 10 (2020) 6356–6366.

[17] J. Ding, Q. Tang, Y. Fu, Y. Zhang, J. Hu, T. Li, Q. Zhong, M. Fan, H.H. Kung, Core-shell covalently linked graphitic carbon nitride-melamine-resorcinol-formaldehyde microsphere polymers for efficient photocatalytic CO_2 reduction to methanol, J. Am. Chem. Soc. 144 (2022) 9576–9585.

[18] Y.J. Sa, C.W. Lee, S.Y. Lee, J. Na, U. Lee, Y.J. Hwang, Catalyst-electrolyte interface chemistry for electrochemical CO_2 reduction, Chem. Soc. Rev. 49 (2020) 6632–6665.

[19] S. Zhang, P. Kang, S. Ubnoske, M.K. Brennaman, N. Song, R.L. House, J.T. Glass, T. J. Meyer, Polyethylenimine-enhanced electrocatalytic reduction of CO_2 to formate at nitrogen-doped carbon nanomaterials, J. Am. Chem. Soc. 136 (2014) 7845–7848.

[20] F. Li, S.F. Zhao, L. Chen, A. Khan, D.R. MacFarlane, J. Zhang, Polyethylenimine promoted electrocatalytic reduction of CO_2 to CO in aqueous medium by graphene-supported amorphous molybdenum sulphide, Energy Environ. Sci. 9 (2016) 216–223.

[21] Y. Han, Y.G. Wang, W. Chen, R. Xu, L. Zheng, J. Zhang, J. Luo, R.A. Shen, Y. Zhu, W.C. Cheong, C. Chen, Q. Peng, D. Wang, Y. Li, Hollow N-doped carbon spheres with isolated cobalt single atomic sites: superior electrocatalysts for oxygen reduction, J. Am. Chem. Soc. 139 (2017) 17269–17272.

[22] Y. Pan, R. Lin, Y. Chen, S. Liu, W. Zhu, X. Cao, W. Chen, K. Wu, W.C. Cheong, Y. Wang, L. Zheng, J. Luo, Y. Lin, Y. Liu, C. Liu, J. Li, Q. Lu, X. Chen, D. Wang, Q. Peng, C. Chen, Y. Li, Design of single-atom Co-N5 catalytic site: a robust electrocatalyst for CO_2 reduction with nearly 100% CO selectivity and remarkable stability, J. Am. Chem. Soc. 140 (2018) 4218–4221.

[23] P. Kuang, Y. Wang, B. Zhu, F. Xia, C.W. Tung, J. Wu, H.M. Chen, J. Yu, Pt single atoms supported on N-doped mesoporous hollow carbon spheres with enhanced electrocatalytic H2-evolution activity, Adv. Mater. 33 (2021) 1–9.

[24] W. Ni, Y. Xue, X. Zang, C. Li, H. Wang, Z. Yang, Y.M. Yan, Fluorine doped cagelike carbon electrocatalyst: an insight into the structure-enhanced CO selectivity for CO_2 reduction at high overpotential, ACS Nano 14 (2020) 2014–2023.

[25] S. Gong, W. Wang, R. Lu, M. Zhu, H. Wang, Y. Zhang, J. Xie, C. Wu, J. Liu, M. Li, S. Shao, G. Zhu, X. Lv, Mediating heterogenized nickel phthalocyanine into isolated Ni-N3 moiety for improving activity and stability of electrocatalytic CO_2 reduction, Appl. Catal. B Environ. 318 (2022), 121813.

[26] F. Xu, B. Ding, Y. Qiu, R. Dong, W. Zhuang, X. Xu, H. Han, J. Yang, B. Wei, H. Wang, S. Kaskel, Generalized domino-driven synthesis of hollow hybrid carbon spheres with ultrafine metal nitrides/oxides, Matter 3 (2020) 246–260.

[27] W. Xiong, H. Li, H. You, M. Cao, R. Cao, Encapsulating metal organic framework into hollow mesoporous carbon sphere as efficient oxygen bifunctional electrocatalyst, Natl. Sci. Rev. 7 (2020) 609–619.

[28] Z. Liu, T. Yan, H. Shi, H. Pan, Y. Cheng, P. Kang, Acidic electrocatalytic CO_2 reduction using space-confined nanoreactors, ACS Appl. Mater. Interfaces 14 (2022) 7900–7908.

[29] J. Du, Y. Xin, M. Dong, J. Yang, Q. Xu, H. Liu, B. Han, Copper/carbon heterogenous interfaces for enhanced selective electrocatalytic reduction of CO_2 to formate, Small 17 (2021) 1–7.

[30] G. Yang, Y. Kuwahara, S. Masuda, K. Mori, C. Louis, H. Yamashita, PdAg nanoparticles and aminopolymer confined within mesoporous hollow carbon spheres as an efficient catalyst for hydrogenation of CO_2 to formate, J. Mater. Chem. A 8 (2020) 4437–4446.

[31] Z.A. Qiao, P. Zhang, S.H. Chai, M. Chi, G.M. Veith, N.C. Gallego, M. Kidder, S. Dai, Lab-in-a-shell: encapsulating metal clusters for size sieving catalysis, J. Am. Chem. Soc. 136 (2014) 11260–11263.

[32] W. Zhang, S. Yang, M. Jiang, Y. Hu, C. Hu, X. Zhang, Z. Jin, Nanocapillarity and nanoconfinement effects of pipet-like bismuth@carbon nanotubes for highly efficient electrocatalytic CO_2 reduction, Nano Lett. 21 (2021) 2650–2657.

[33] J. Yuan, S. Chen, Y. Zhang, R. Li, J. Zhang, T. Peng, Structural regulation of coupled phthalocyanine–porphyrin covalent organic frameworks to highly active and selective electrocatalytic CO_2 reduction, Adv. Mater. 34 (2022) 1–11.

[34] L. Yang, H. Li, Y. Yu, Y. Wu, L. Zhang, Assembled 3D MOF on 2D nanosheets for self-boosting catalytic synthesis of N-doped carbon nanotube encapsulated metallic Co electrocatalysts for overall water splitting, Appl. Catal. B Environ. 271 (2020), 118939.

[35] N. Zhang, X. Zhang, L. Tao, P. Jiang, C. Ye, R. Lin, Z. Huang, A. Li, D. Pang, H. Yan, Y. Wang, P. Xu, S. An, Q. Zhang, L. Liu, S. Du, X. Han, D. Wang, Y. Li, Silver single-atom catalyst for efficient electrochemical CO_2 reduction synthesized from thermal transformation and surface reconstruction, Angew. Chem. Int. Ed. 60 (2021) 6170–6176.

[36] X. Jiang, L. Zhang, H. Liu, D. Wu, F. Wu, L. Tian, L. Liu, J. Zou, S. Luo, B. Chen, Silver single atom in carbon nitride catalyst for highly efficient photocatalytic hydrogen evolution, Angew. Chem. 132 (2020) 23312–23316.

[37] J. Li, W. Tang, H. Yang, Z. Dong, J. Huang, S. Li, J. Wang, J. Jin, J. Ma, Enhanced-electrocatalytic activity of $Ni_{1-x}Fe_x$ alloy supported on polyethyleneimine functionalized MoS_2 nanosheets for hydrazine oxidation, RSC Adv. 4 (2014) 1988–1995.

[38] B. Debret, B. Ménez, B. Walter, H. Bouquerel, P. Bouilhol, N. Mattielli, C. Pisapia, T. Rigaudier, H.M. Williams, High-pressure synthesis and storage of solid organic compounds in active subduction zones, Sci. Adv. 8 (2022) eabo2397.

[39] X. Wang, X. Ma, L. Sun, C. Song, A nanoporous polymeric sorbent for deep removal of H_2S from gas mixtures for hydrogen purification, Green Chem. 9 (2007) 695–702.

[40] S. Bali, T.T. Chen, W. Chaikittisilp, C.W. Jones, Oxidative stability of amino polymer-alumina hybrid adsorbents for carbon dioxide capture, Energy Fuels 27 (2013) 1547–1554.

[41] K. Kong, S. Zhang, Y. Chu, Y. Hu, F. Yu, H. Ye, H. Ding, J. Hua, A self-assembled perylene diimide nanobelt for efficient visible-light-driven photocatalytic H_2 evolution, Chem. Commun. 55 (2019) 8090–8093.

[42] S. Hanselman, M.T.M. Koper, F. Calle-Vallejo, Computational comparison of late transition metal (100) surfaces for the electrocatalytic reduction of CO to C_2 species, ACS Energy Lett. 3 (2018) 1062–1067.

[43] K.P. Kuhl, T. Hatsukade, E.R. Cave, D.N. Abram, J. Kibsgaard, T.F. Jaramillo, Electrocatalytic conversion of carbon dioxide to methane and methanol on transition metal surfaces, J. Am. Chem. Soc. 136 (2014) 14107–14113.

[44] J. Li, H. Xiong, X. Liu, D. Wu, D. Su, B. Xu, Q. Lu, Weak CO binding sites induced by Cu-Ag interfaces promote CO electroreduction to multi-carbon liquid products, Nat. Commun. 14 (2023) 698.

[45] Y. Liu, D. Tian, A.N. Biswas, Z. Xie, S. Hwang, J.H. Lee, H. Meng, J.G. Chen, Transition metal nitrides as promising catalyst supports for tuning CO/H_2 syngas production from electrochemical CO_2 reduction, Angew. Chem. Int. Ed. 59 (2020) 11345–11348.

[46] W. Wang, X. He, K. Zhang, Y. Yao, Surfactant-modified Zn nanosheets on carbon paper for electrochemical CO_2 reduction to CO, Chem. Commun. 58 (2022) 5096–5099.

[47] Y. Kuwahara, H. Kango, H. Yamashita, Pd Nanoparticles and Aminopolymers confined in hollow silica spheres as efficient and reusable heterogeneous catalysts for semihydrogenation of alkynes, ACS Catal. 9 (2019) 1993–2006.

[48] F. Lei, W. Liu, Y. Sun, J. Xu, K. Liu, L. Liang, T. Yao, B. Pan, S. Wei, Y. Xie, Metallic tin quantum sheets confined in graphene toward high-efficiency carbon dioxide electroreduction, 7 (2016) 1–8.

[49] L. Xue, C. Zhang, T. Shi, S. Liu, H. Zhang, M. Sun, F. Liu, Y. Liu, Y. Wang, X. Gu, S. Zeng, Unraveling the improved CO_2 adsorption and COOH* formation over Cu-decorated ZnO nanosheets for CO_2 reduction toward CO, Chem. Eng. J. 452 (2023), 139701.

[50] L.P. Yuan, W.J. Jiang, X.L. Liu, Y.H. He, C. He, T. Tang, J. Zhang, J.S. Hu, Molecularly engineered strong metal oxide-support interaction enables highly efficient and stable CO_2 electroreduction, ACS Catal. 10 (2020) 13227–13235.

[51] C. Chen, X. Sun, X. Yan, Y. Wu, M. Liu, S. Liu, Z. Zhao, B. Han, A strategy to control the grain boundary density and Cu^+/Cu^0 ratio of Cu-based catalysts for efficient electroreduction of CO_2 to C_2 products, Green Chem. 22 (2020) 1572–1576.

[52] J.J. Masana, J. Xiao, H. Zhang, X. Lu, M. Qiu, Y. Yu, Nitrogen-rich carbon nitride inducing electron delocalization of Co-N_4 site to enhance electrocatalytic carbon dioxide reduction, Appl. Catal. B Environ. 323 (2023), 122199.

[53] Z. Chen, H. Hu, L. Yin, Z. Zhao, J.-H. Choi, G. Liu, F. Geng, Composite non-noble system with bridging oxygen for catalyzing Tafel-type alkaline hydrogen evolution, Proc. Natl. Acad. Sci. 120 (2023) 2017.

[54] P. Chen, P. Zhang, X. Kang, L. Zheng, G. Mo, R. Wu, J. Tai, B. Han, Efficient electrocatalytic reduction of CO_2 to ethane over nitrogen-doped Fe_2O_3, J. Am. Chem. Soc. 144 (2022) 14769–14777.